photonics

MDPI

Communication

Dynamical Modulation of Transverse Orbital Angular Momentum in Highly Confined Spatiotemporal Optical Vortex

Jian Chen [1,2,3,*], Siyu Kuai [1], Guoliang Chen [1], Lihua Yu [1] and Qiwen Zhan [1,2,3,*]

[1] School of Optical-Electrical and Computer Engineering, University of Shanghai for Science and Technology, Shanghai 200093, China
[2] Shanghai Key Laboratory of Modern Optical System, University of Shanghai for Science and Technology, Shanghai 200093, China
[3] Zhangjiang Laboratory, 100 Haike Road, Shanghai 201204, China
* Correspondence: cj@usst.edu.cn (J.C.); qwzhan@usst.edu.cn (Q.Z.)

Abstract: Spatiotemporal optical vortices (STOVs) have attracted numerous attention from researchers in recent years due to their intriguing characteristics with transverse orbital angular momentum (OAM) in the spatiotemporal domain. In this work, we numerically analyze the tightly focusing characteristics of higher-order STOVs and present a method to dynamically modulate the transverse OAM in highly confined STOVs. Richards–Wolf vectorial diffraction theory was employed to simulate the three-dimensional spatiotemporal distribution of the focused STOV corresponding to the incident wave packet of topological charge of −2. The simulation results show that the higher-order spatiotemporal vortices in the transversely polarized components of the focused wave packets split into two first-order vortices with topological charge of −1 when the waist radius of the incident wave packet was larger than 40% of the pupil radius of the focusing lens, and the spacing of the two split vortices could be tailored by adjusting the waist radius of the incident wave packet. Meanwhile, the incident spatial waist radius also affected the tilt angle of the phase singularity trace in the z-polarized component of the focused field. The presented method provides a flexible way to dynamically engineer the spatiotemporal vortices in the tightly focused wave packet and may find potential applications in nanophotonics, light–matter interaction, quantum information processing, etc.

Keywords: spatiotemporal optical vortex; transverse orbital angular momentum; spiral phase; tightly focusing

Citation: Chen, J.; Kuai, S.; Chen, G.; Yu, L.; Zhan, Q. Dynamical Modulation of Transverse Orbital Angular Momentum in Highly Confined Spatiotemporal Optical Vortex. *Photonics* **2023**, *10*, 148. https://doi.org/10.3390/photonics10020148

Received: 12 January 2023
Revised: 28 January 2023
Accepted: 30 January 2023
Published: 31 January 2023

1. Introduction

Photons can carry both linear momentum and angular momentum, where the angular momentum can be further divided into spin angular momentum (SAM) and orbital angular momentum (OAM). SAM is associated with the circular polarization of light, while OAM is linked with the spiral phase distribution, forming the so-called optical vortex. Optical vortex beams with phase singularities and null intensities at their center are well-established phenomena in modern singular optics, first discovered in 1992 by Allen et al. [1], which can be applied in optical communication [2–4], quantum information [5,6], super-resolution microscopic imaging [7,8], micro-/nanoparticle trapping [9,10], and quantum key distribution [11].

Traditionally, the research on vortices has mainly focused on longitudinal OAM in the spatial domain, whose axis is parallel to the propagation direction of the beam. A two-mode fiber-based beam converter is adopted to create optical vector beams with embedded optical vortices from the incident linearly polarized Gaussian beam [12]. As for fractional vortex beams with half-integer topological charge values, a vortex chain of alternating charges can be observed along the radial phase discontinuity line [13,14]. High-order optical vortex lattices with controllable arbitrary modes are experimentally

generated and the topological charge on each optical vortex in the lattice is up to 51 [15]. Based on the pulse-width approximation of Bessel functions, an improved method with a notable simplicity in its practical realization is presented to create the perfect optical vortex [16]. Attosecond extreme ultraviolet vortices can be generated by exploiting the high-order harmonic generation and propagation of infrared fields carrying OAM [17].

By introducing temporal phase variation, one can generate a spatiotemporal optical vortex with transverse OAM. For example, the interaction of two non-coplanar phase-modulated beams will lead to a train of spatiotemporal vortices [18]. Based on the Klein–Gordon wave equations, generic STOVs are constructed with intrinsic OAM oriented along an arbitrary direction [19]. Thereafter, STOVs are experimentally observed during extremely high-powered short pulse collapse and filamentation in air [20]. Recently, a linear method was presented to experimentally generate STOVs by employing a 4f pulse shaper [21,22]. Subsequently, the local densities and integral values of the SAM and OAM of both the scalar and vector Bessel-type STOVs were calculated and the spin–orbit interactions in the transverse spin and orbital angular momentums were predicted [23]. Furthermore, the experimental generation of the second harmonic of STOV pulses has been conducted to reveal the conservation of transverse OAM in such a process [24,25]. The generation and propagation of STOVs has theoretically been analyzed step-by-step on a basis of diffraction theory [26]. A class of models was developed to analyze the propagation of STOVs in dispersive media, revealing that the STOV symmetry and the group velocity dispersion would lead to the quantization of transverse OAM [27]. A space-to-time mapping technique was demonstrated to directly modulate the spatiotemporal phase to chirped pulses by utilizing the relationship between frequency and time [28]. Cylindrically polarized STOVs have been experimentally generated to demonstrate the coexistence of spatiotemporal phase singularities with spatial polarization singularities [29]. A preconditioning method was proposed to overcome the spatiotemporal astigmatism effect of the high numerical aperture (NA) lens to create highly confined STOVs with near diffraction-limited sizes [30]. Dynamic STOVs have also been demonstrated by embedding two spatiotemporal vortices with different transverse OAMs in one wave packet [31]. The spin–orbit interaction between the longitudinal SAM and transverse OAM in tightly focused circularly polarized STOVs could produce intriguing complex spatiotemporal phase singularity structures [32]. Novel types of transverse and longitudinal pulse shifts caused by transverse OAM have theoretically been observed in the reflection and refraction of STOVs at a planar isotropic interface [33]. Spatiotemporal vortices with arbitrarily oriented OAM are generated by employing a compact photonic crystal slab with transmission nodal lines in 3D wavevector–frequency space [34]. Based on spatially resolved spectral interferometry, a simple single-frame method was developed to quantitatively characterize STOVs to identify their topological charge numbers, OAM helicity, pulse dispersions, and beam divergences [35].

Further understanding of the physical properties of STOVs, for example, the tight focusing of higher-order STOVs, is important for both theoretical research and practical applications. In this paper, we studied the dynamic modulation of transverse OAM in the tight focusing of right-handed circularly polarized (RCP) STOVs with topological charge of -2. To prevent the collapse of the transverse OAM in the focal plane of the high NA lens, the incident wave packet was preconditioned based on the approach similar to the cylindrical lens mode converter. The effect of the spatial waist of the incident wave packet on the vortices splitting in the tightly focused field was analyzed in detail by employing the Richards–Wolf vectorial diffraction theory. The second-order vortices in the focused field will split into two first-order vortices as the spatial waist of the incident wave packet exceeds a threshold. By adjusting the spatial waist of the incident wave packet, the spacing of the two split STOVs in a highly confined field could be tailored in a controllable way. The presented method provides an effective way to achieve fast modulation of transverse OAM in a highly confined field.

2. Methods

To recover the spatiotemporal spiral phase in the focal plane of the high NA lens, we needed to precondition the incident wave packet to overcome the spatiotemporal astigmatism caused by the tightly focusing system. Inspired by the Hermite–Gaussian modes can be decomposed into a linear superposition of Laguerre–Gaussian modes, the RCP STOV with topological charge of −2 could be preconditioned as:

$$\begin{aligned} \boldsymbol{E}_t^{-2}(x,y,t) &= -i\left[\boldsymbol{E}_{02}^{LG}(x,y,t) - \boldsymbol{E}_{20}^{LG}(x,y,t)\right] - \boldsymbol{E}_{11}^{LG}(x,y,t) \\ &= \frac{\sqrt{2}}{2}\begin{pmatrix} \boldsymbol{e}_x \\ i\boldsymbol{e}_y \end{pmatrix}\left[2\left(\frac{x}{w}+\frac{t}{w_t}\right)^2 - 1\right]\exp\left(-\frac{x^2+y^2}{w^2} - \frac{t^2}{{w_t}^2}\right) \end{aligned} \tag{1}$$

where $\boldsymbol{e}_x$, $\boldsymbol{e}_y$ are the unit vectors along the x- and y-axes, w is the spatial waist radius of the incident wave packet, and w_t is the pulse half-width at $1/e^2$ of the maximum intensity of the wave packet in the temporal domain. $\boldsymbol{E}_{02}^{LG}(x,y,t)$, $\boldsymbol{E}_{20}^{LG}(x,y,t)$, and $\boldsymbol{E}_{11}^{LG}(x,y,t)$ can be given by the following expressions:

$$\begin{aligned} \boldsymbol{E}_{02}^{LG}(x,y,t) &== \frac{\sqrt{2}}{2}\begin{pmatrix} \boldsymbol{e}_x \\ i\boldsymbol{e}_y \end{pmatrix}\left[\left(\frac{x}{w}+\frac{it}{w_t}\right)^2\right]\exp\left(-\frac{x^2+y^2}{w^2} - \frac{t^2}{{w_t}^2}\right) \\ \boldsymbol{E}_{20}^{LG}(x,y,t) &== \frac{\sqrt{2}}{2}\begin{pmatrix} \boldsymbol{e}_x \\ i\boldsymbol{e}_y \end{pmatrix}\left[\left(\frac{x}{w}-\frac{it}{w_t}\right)^2\right]\exp\left(-\frac{x^2+y^2}{w^2} - \frac{t^2}{{w_t}^2}\right) \\ \boldsymbol{E}_{11}^{LG}(x,y,t) &== \frac{\sqrt{2}}{2}\begin{pmatrix} \boldsymbol{e}_x \\ i\boldsymbol{e}_y \end{pmatrix}\left[-2\left(\frac{x^2}{w^2}+\frac{t^2}{w_t^2}\right)+1\right]\exp\left(-\frac{x^2+y^2}{w^2} - \frac{t^2}{{w_t}^2}\right) \end{aligned} \tag{2}$$

The spatiotemporal distribution of the preconditioned RCP incident wave packet is shown in Figure 1. From Figure 1a–c, we can see that all the wave packets of the x-, y-polarized components and the entire incident pulse are split into three detached parts, similar to the HG_{20} mode. Meanwhile, the wave packets are rotated by 45 degrees with regard to the t-axis in the x–t plane. As shown in Figure 1d,e, the phase of the x-polarized component was binarized into 0 (green areas) and π (yellow areas), while the phase of the y-polarized component was binarized into π/2 (brown areas) and –π/2 (blue areas). From Figure 1f, we can see that the incident wave packet was right-handed and circularly polarized in the spatial domain, since the polarization ellipses are circular and black.

The above preconditioned incident wave packet was tightly focused by a high NA lens to obtain highly confined STOVs, as shown in Figure 2. Therefore, the Richards–Wolf vectorial diffraction formula could be utilized to calculate the focused wave packet on the focal plane of the lens, which can be expressed as [36]:

$$\begin{aligned} \boldsymbol{E}_f\left(r_f,\Phi,z_f,t\right) &= \int_0^{\alpha}\int_0^{2\pi}\boldsymbol{P}(\theta,\phi)B(\theta)E_\Omega(\theta,\phi,t) \\ &\quad\times\exp\left\{-ik\left[r_f\sin\theta\cos(\phi-\Phi)+z_f\cos\theta\right]\right\}\sin\theta d\theta d\phi \end{aligned} \tag{3}$$

where α is the convergence half angle of the focusing lens, $r_f = \sqrt{x_f^2+y_f^2}$, $z_f = 0$, $\Phi = \tan^{-1}(y_f/x_f)$, $\boldsymbol{P}(\theta,\phi)$ is the polarization distribution of the refracted field on the spherical surface Ω, and $B(\theta)$ is the apodization function of the objective lens. Here, the sine condition lens was used and $B(\theta) = \sqrt{\cos\theta}$. $k = 2\pi/\lambda$ is the wave number and λ is the center wavelength of the incident wave packet. $E_\Omega(\theta,\ \phi,t)$ is the complex optical field on the spherical surface Ω, which can be given by:

$$E_\Omega(\theta,\phi,t) = \frac{\sqrt{2}}{2}e^{i\phi}\left[2\left(\frac{\sin\theta\cos\phi}{w}+\frac{t}{w_t}\right)^2 - 1\right]\exp\left(-\frac{\sin^2\theta}{w^2} - \frac{t^2}{w_t^2}\right) \tag{4}$$

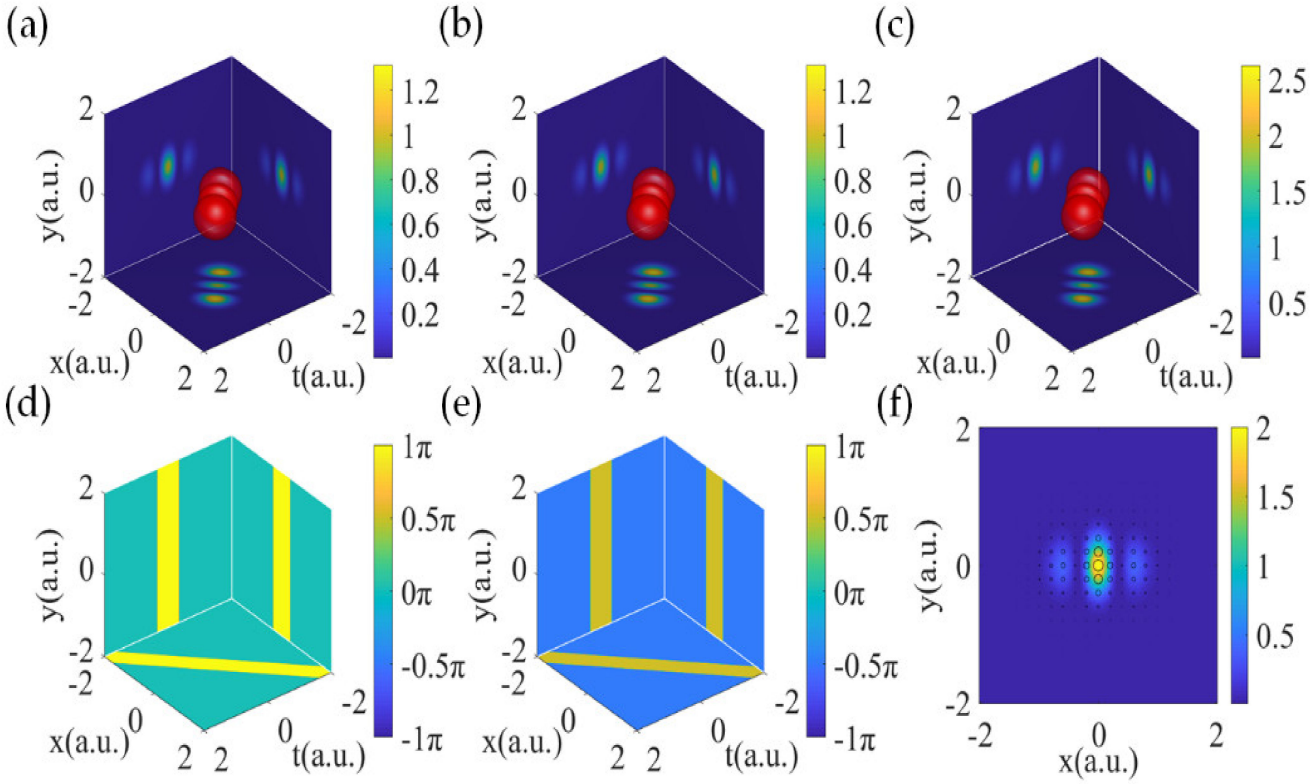

Figure 1. The preconditioned RCP incident wave packet. (**a**) The intensity distributions of the x-polarized component on the three orthogonal planes, combined with an isosurface at 10% of its peak intensity. (**b**) The intensity distributions of the y-polarized component on the three orthogonal planes, combined with an isosurface at 10% of its peak intensity. (**c**) The intensity distributions of the entire incident wave packet on the three orthogonal planes, combined with an isosurface at 10% of its peak intensity. (**d**) The phase distribution of the x-polarized component on the three orthogonal planes. (**e**) The phase distribution of the y-polarized component on the three orthogonal planes. (**f**) The polarization distribution of the preconditioned incident wave packet in the x–y plane.

Considering the polarization direction change of the radially polarized component in the incident RCP wave packet caused by the high NA lens, the polarization distribution $\boldsymbol{P}(\theta, \phi)$ of the refracted beam can be derived as:

$$\boldsymbol{P}(\theta,\phi) = \begin{pmatrix} (\cos\theta\cos\phi - i\sin\phi)\cdot \boldsymbol{e}'_x \\ (\cos\theta\sin\phi + i\cos\phi)\cdot \boldsymbol{e}'_y \\ \sin\theta\cdot \boldsymbol{e}'_z \end{pmatrix} \tag{5}$$

where $\boldsymbol{e}'_x$, $\boldsymbol{e}'_y$, and $\boldsymbol{e}'_z$ are the three unit vectors along the Cartesian coordinates in the focal region of the lens.

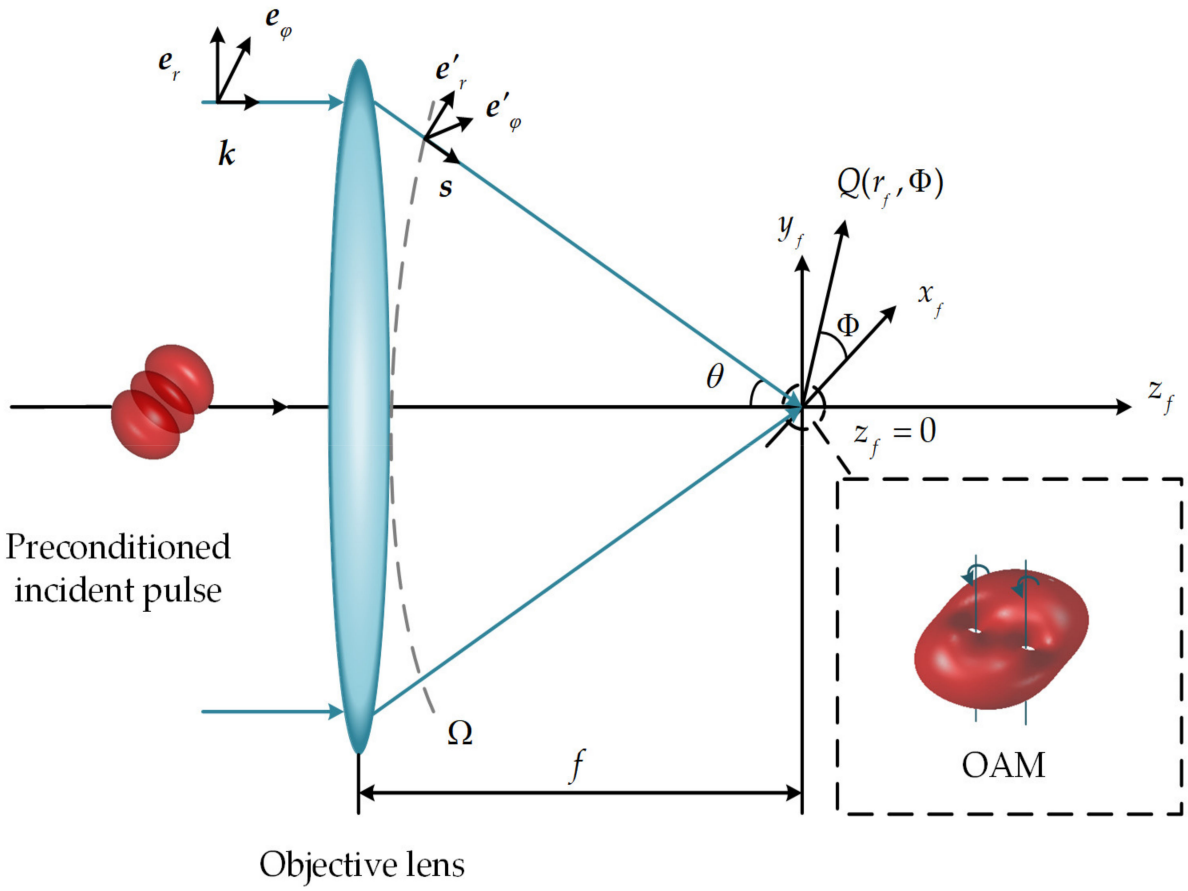

Figure 2. Schematic diagram of tightly focusing the incident wave packet. $Q\left(r_f, \Phi\right)$ is an arbitrary observation point on the focal plane of the lens. The inset illustrates the splitting of the second-order STOV into two first-order STOVs.

3. Results

In the following simulations, the spatial size and temporal size of the incident wave packets were normalized to the pupil radius of the high NA lens and the pulse half-width, respectively. Moreover, NA = 0.9 was adopted in all the simulations. Since w_t has no effect on the vortex spacing in the focal field, we thus kept w_t as 0.5 in the following simulations.

3.1. Transversely Polarized Components

To reveal the effect of the incident spatial waist radius w on the vortex spacing in the transversely polarized components of the focused STOVs, we present the intensity and phase distributions of the x- and y-polarized components of the focused STOVs corresponding to incident spatial waist radii of 0.3, 0.5, and 0.7, as shown in Figures 3 and 4. When w was 0.3, from Figure 3a, we can see that there only existed one phase singularity trace in the wave packet along the y-axis for the x-polarized component of the focused field. Meanwhile, according to Figure 3d, the spiral phase in the x–t plane changed anti-clockwise in the range [$-\pi$, π] for two times, indicating that the x-polarized component of the focused wave packet carried transverse OAM of topological charge of -2. In other words, the transverse vortex in the focused x-polarized component did not split. For the y-polarized component of the focused field, as shown in Figure 4a,d, the transverse vortex also did not split and carried transverse OAM of topological charge of -2 in the x–t plane as well. When w was increased to 0.5, according to Figure 3b, we can see that there occurred two phase singularity traces in the wave packet of the x-polarized component of the focused field along the y-axis. Based on the phase distribution in Figure 3e, we can see that there existed two phase singularities in the x–t plane. The spiral phase around each singularity changed

anti-clockwise in the range [–π, π] once, indicating that the high-order STOV split into two STOVs with topological charge of −1. The coordinates of the two phase singularities in the x–t plane were found to be (−0.04, 0.12) and (0.04, 0.12). Thus, the spacing between the two transverse vortices was 0.24 a.u. along the t-axis and 0.08 λ along the x-axis. As for the y-polarized component, from Figure 4b,e, the high-order STOV also split into two first-order STOVs with topological charge of −1. The coordinates of the two phase singularities were evaluated to be (−0.12, −0.12) and (0.12, 0.12). Therefore, the spacing between them was 0.24 a.u. along the t-axis and 0.24 λ along the x-axis. When w was further increased to 0.7, as shown in Figure 3c,f, the higher-order STOV in the x-polarized component of the focused field also split into two first-order STOVs with topological charge of −1. Furthermore, the spacing between them was enlarged to 0.64 a.u. along the t-axis, while their spacing was 0 along the x-axis, since the coordinates of the two phase singularities were found to be (0, −0.32) and (0, 0.32). For the y-polarized component of the focused field, according to Figure 4c,f, the coordinates of the two phase singularities were determined to be (−0.2, −0.32) and (0.2, 0.32); thus, the spacing between the two first-order STOVs was enlarged to 0.64 a.u. along the t-axis and 0.4 λ along the x-axis.

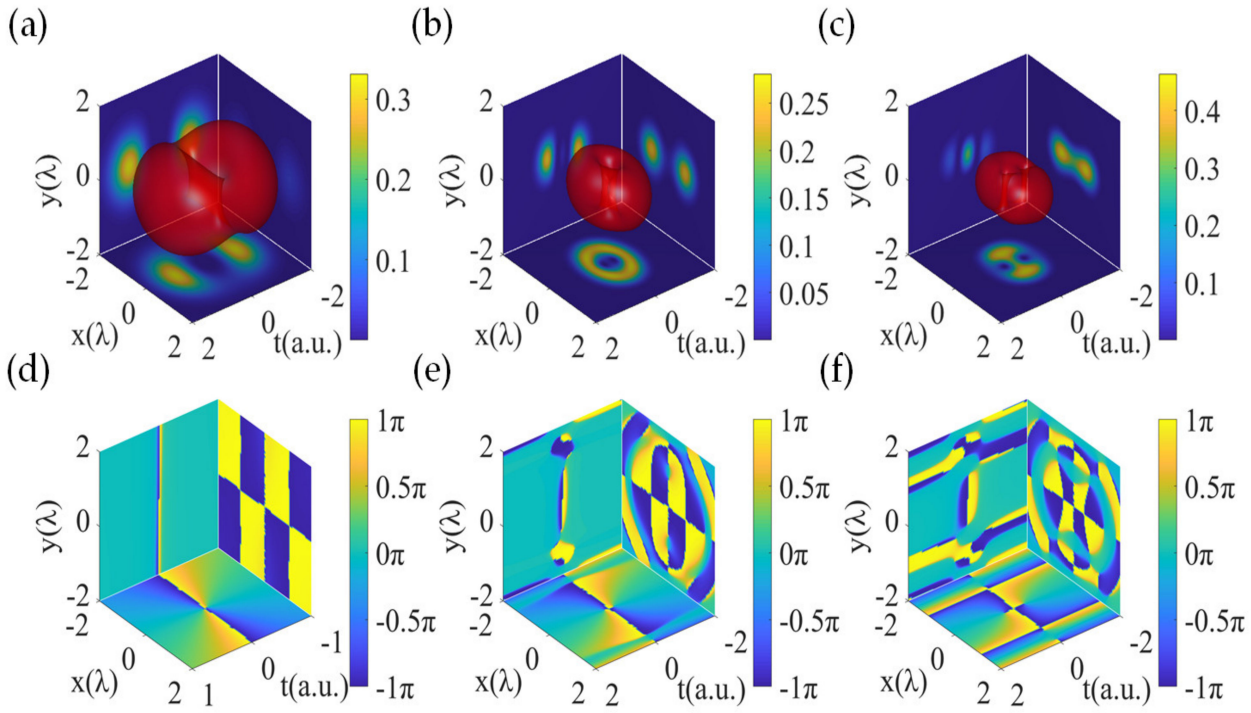

Figure 3. The intensity and phase distributions of the x-polarized components of the focused STOVs under different incident spatial waist radii. (**a**–**c**) The intensity distributions of the x-polarized components of the focused STOVs corresponding to incident spatial waist radii of 0.3, 0.5, and 0.7, respectively. (**d**–**f**) The phase distributions corresponding to the three cases, respectively. The isosurfaces are depicted at 5% of the maximum intensity in each case.

To further analyze the variation rule of the focused STOVs in the transversely polarized components caused by the incident spatial waist radius, w was changed from 0.2 to 0.9 with ste of 0.1. The spacing between the focused STOVs was calculated in each case and the results are shown in Figure 5. Figure 5a,b presents the spacing variation between the STOVs in the x-polarized component of the focused field along the x-axis and t-axis, respectively. Meanwhile, Figure 5c,d gives the spacing variation in the y-polarized component of the focused field along the x-axis and t-axis, respectively. We can see that when w was less than 0.4, the spacing along the x-axis and t-axis was 0 for both the x-polarized component and y-polarized component, indicating the second-order STOV did not split. When w was

larger than 0.4, the second-order STOV split into two first-order STOVs for both the x- and y-polarized components, and the spacing between the two first-order STOVs along the t-axis almost linearly increased as w increased. The spatial waist of the incident wave packet had less of an effect on the spacing along the x-axis for the x-polarized component compared to that of the y-polarized component. It should be pointed out that the incident spatial waist radius was normalized by the pupil radius of the high NA lens; thus, the horizontal axes in Figure 5a–d represent the ratio between the spatial waist radius of the incident wave packet and the pupil radius of the high NA lens.

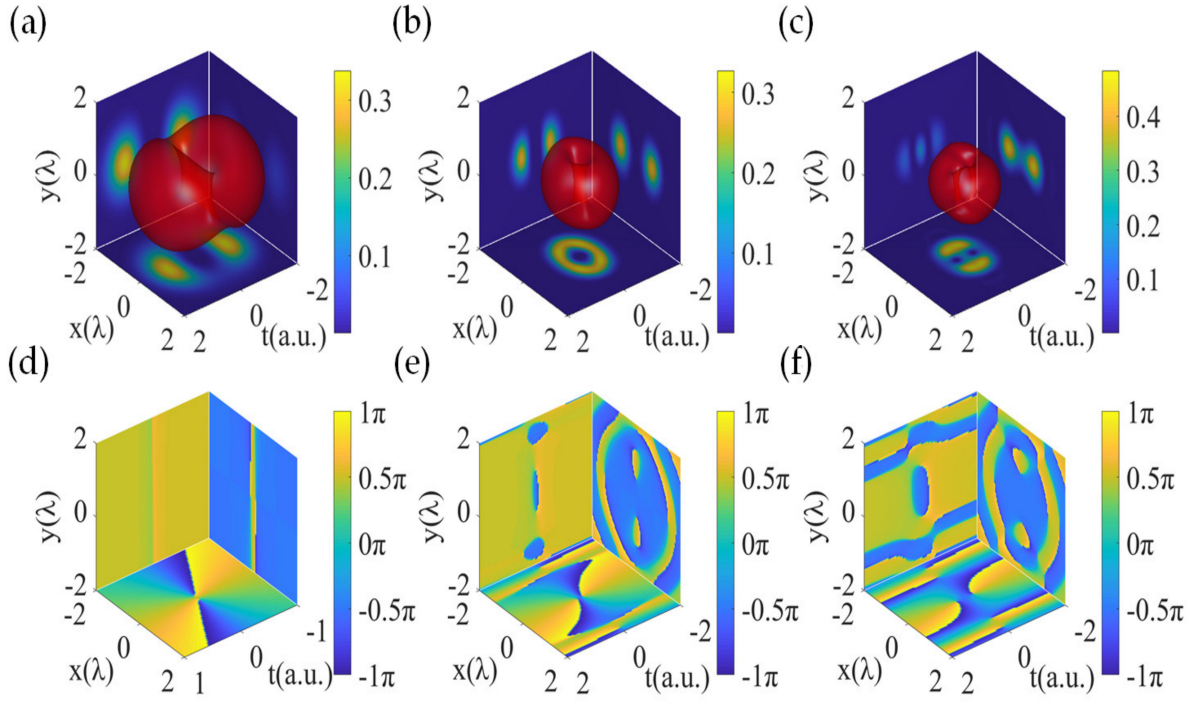

Figure 4. The intensity and phase distributions of the y-polarized components of the focused STOVs under different incident spatial waist radii. (**a**–**c**) The intensity distributions of the y-polarized components of the focused STOVs corresponding to incident spatial waist radii of 0.3, 0.5, and 0.7, respectively. (**d**–**f**) The phase distributions corresponding to the three cases, respectively. The isosurfaces are depicted at 5% of the maximum intensity in each case.

3.2. Longitudinally Polarized Components

To investigate the effect of the incident spatial waist radius w on the OAM in the z-polarized component of the focused wave packet, we also set w to be 0.3, 0.5, and 0.7 and calculated the three-dimensional spatiotemporal distribution of the z-polarized component of the focal field in each case. The results are shown in Figure 6, from which we can see the OAM in the z-polarized component exhibited a more complex spatiotemporal structure. According to the intensity distribution in the y–t plane shown in Figure 6a–c, there existed a phase singularity trace in the center of the wave packet in each case, and the phase singularity trace was tilted as the incident spatial waist radius w increased. Correspondingly, there exists an abrupt phase variation line in the y–t plane, as shown in Figure 6d–f. Assuming the central wavelength of the wave packet was 1 μm and the pulse half-width was 10 fs, the tilt angles of the phase singularity trace in the three cases were evaluated to be 0°, 7.43°, and 40.03°, indicating that an increase in w significantly affected the tilt angle of the phase singularity trace in the z-polarized component.

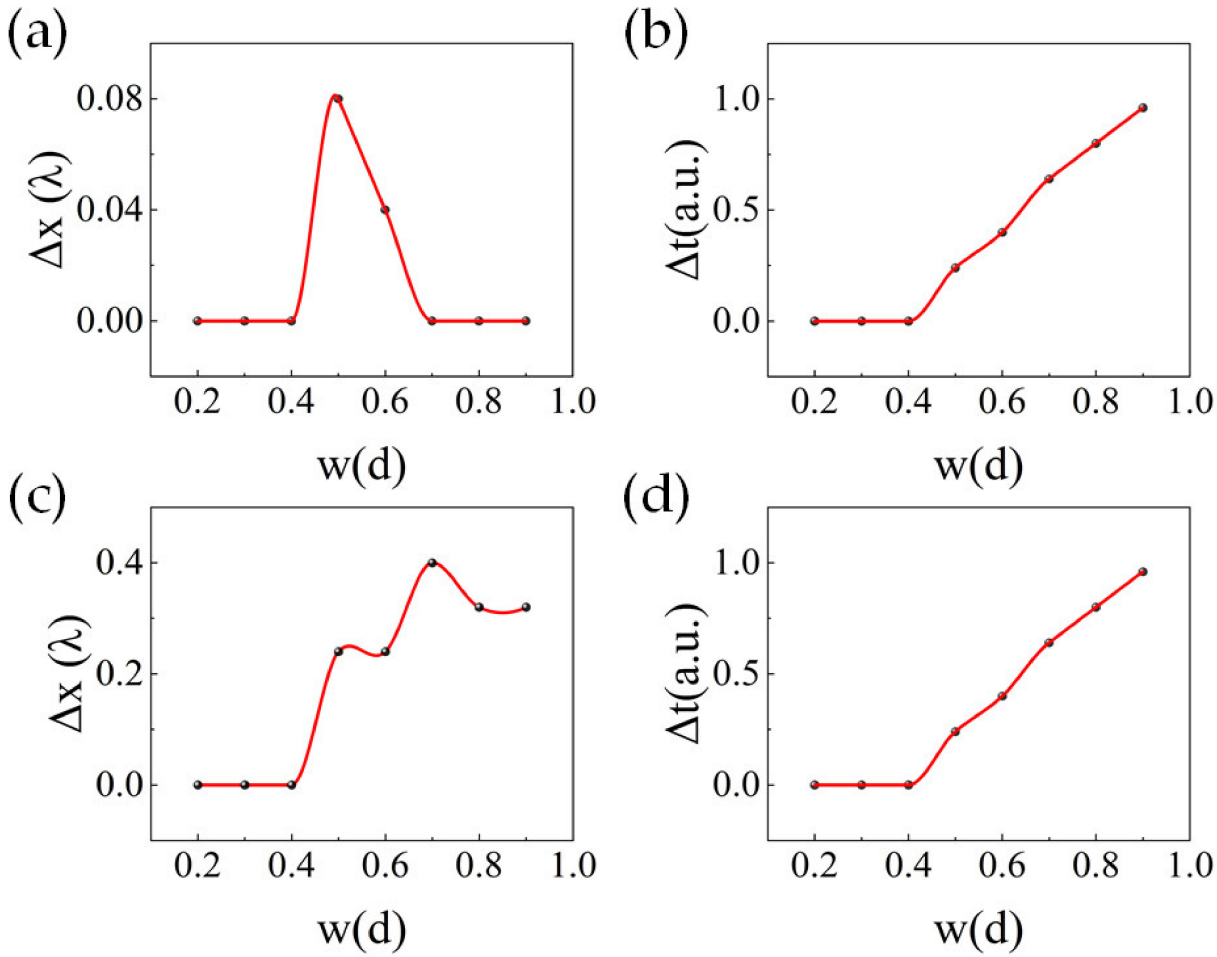

Figure 5. The relationship between the vortex spacing in the transversely polarized components of the focused wave packet and the incident spatial waist radius. (**a**) Vortex spacing of the x-polarized component along the x-axis in the focal region. (**b**) Vortex spacing of the x-polarized component along the t-axis in the focal region. (**c**) Vortex spacing of the y-polarized component along the x-axis in the focal region. (**d**) Vortex spacing of the y-polarized component along the t-axis in the focal region. The *d* in the horizontal axis in each subfigure represents the pupil radius of the high NA lens.

To reveal the relationship between the tilt angle of the phase singularity trace in the z-polarized component and the incident spatial waist radius w, we changed w in the range [0.2, 0.9] with step of 0.1 and calculated the tilt angle in each case. The results are shown in Figure 7. Obviously, when the incident spatial waist w was less than 0.4, the tilt angle was kept as 0°, indicating that transverse OAM was predominant in that case. When the incident spatial waist w was larger than 0.4, the tilt angle increased almost linearly as w increased. Thus, the tilt angle of the phase singularity trace in the z-polarized component of the focal field could be controlled by just changing the spatial waist radius of the incident wave packet.

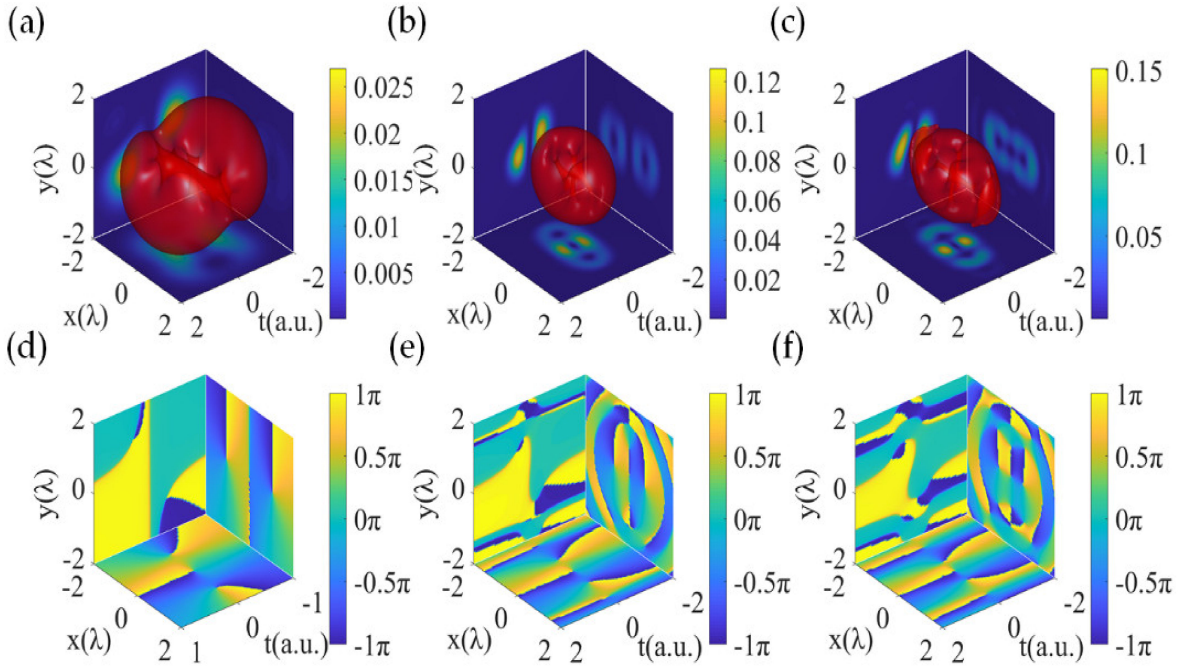

Figure 6. The intensity and phase distributions of the z-polarized components of the focused STOVs under different incident spatial waist radii. (**a**–**c**) The intensity distributions of the z-polarized components of the focused STOVs corresponding to incident spatial waist radii of 0.3, 0.5, and 0.7, respectively. (**d**–**f**) The phase distributions corresponding to the three cases, respectively. The isosurfaces are depicted at 3% of the maximum intensity in each case.

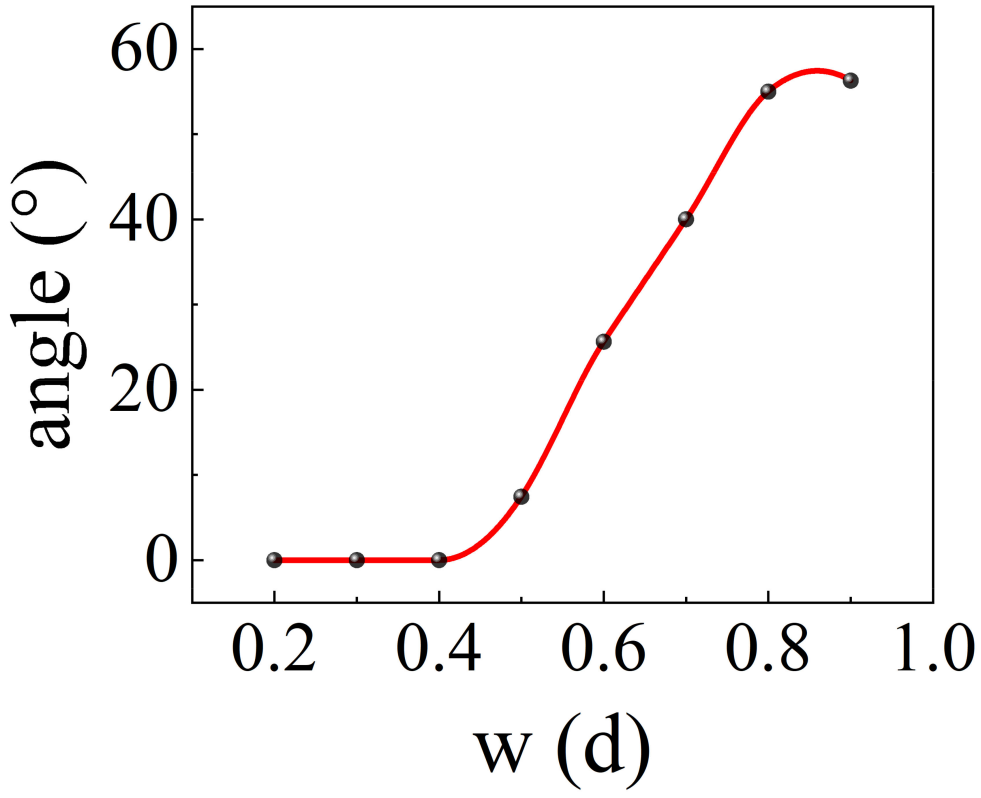

Figure 7. The relationship between the tilt angle of the phase singularity trace in the z-polarized component of the focused field and the incident spatial waist radius. The *d* in the horizontal axis represents the pupil radius of the high NA lens.

4. Discussion

In summary, we studied the effect of the incident spatial waist radius on the OAM in tightly focusing high-order RCP STOVs carrying transverse OAM with topological charge of -2. For the transversely polarized components in the focused field, the second-order STOV split into two first-order STOVs as the incident spatial waist radius increased over 40% of the pupil radius of the focusing lens, and the spacing between the two first-order STOVs along the t-axis exhibited a linear relationship with the incident spatial waist radius. Moreover, the incident spatial waist radius had a smaller effect on the spacing between the two first-order STOVs along the x-axis in the x-polarized component than that in the y-polarized component. For the longitudinally polarized component of the focused field, the incident spatial waist radius led to the tilt of the phase singularity trace in the wave packet as it increased beyond 40% of the pupil radius of the focusing lens. The presented results provide a feasible method to dynamically tailor STOVs in highly confined wave packets with controllable vortex spacing and a phase singularity trace tilt angle, which may find applications in optical tweezers, spin–orbit coupling, light–matter interactions, and so on. Since there exists transverse OAM in highly confined STOVs, they could provide an additional degree of freedom for the optical tweezer to manipulate the nanoparticle or nanostructure. For example, it may make the nanoobject orbit in the meridian plane which is orthogonal to the propagation direction of the beam. The two split first-order STOVs may make it possible to simultaneously trap nanoobjects in two different locations. On the other hand, considering the complicated OAM structure in the z-component of the focused wave packet, if the sample selectively responds to the state of z-polarization, it could then be possible to create photon emissions with specific SAM and OAM states by using highly confined vectorial STOVs.

Author Contributions: Conceptualization, J.C.; investigation, J.C., S.K. and L.Y.; methodology, J.C. and Q.Z.; software, J.C. and S.K.; validation, J.C. and Q.Z.; formal analysis, J.C., S.K., G.C. and L.Y.; writing—original draft preparation, S.K. and G.C.; writing—review and editing, J.C. and Q.Z.; visualization, S.K.; supervision, J.C.; project administration, J.C. and Q.Z.; funding acquisition, J.C. and Q.Z. All authors have read and agreed to the published version of the manuscript.

Funding: This research was funded by the National Natural Science Foundation of China (Grant Nos. 12274299, 92050202, 12204309); Shanghai Science and Technology Committee (Grant No. 22QA1406600); and Shanghai Natural Science Foundation (Grant No. 20ZR1437600).

Institutional Review Board Statement: Not applicable.

Data Availability Statement: The data presented in this study are available upon request from the corresponding author.

Conflicts of Interest: The authors declare no conflict of interest.

References

1. Allen, L.; Beijersbergen, M.W.; Spreeuw, R.J.C.; Woerdman, J.P. Orbital Angular Momentum of Light and the Transformation of Laguerre-Gaussian Laser Modes. *Phys. Rev. A* **1992**, *45*, 8185–8189. [CrossRef]
2. Lei, T.; Zhang, M.; Li, Y.R.; Jia, P.; Liu, G.N.; Xu, X.G.; Li, Z.H.; Min, C.J.; Lin, J.; Yu, C.Y.; et al. Massive Individual Orbital Angular Momentum Channels for Multiplexing Enabled by Dammann Gratings. *Light Sci. Appl.* **2015**, *4*, e257. [CrossRef]
3. Gong, L.; Zhao, Q.; Zhang, H.; Hu, X.Y.; Huang, K.; Yang, J.M.; Li, Y.M. Optical orbital-angular-momentum multiplexed data transmission under high scattering. *Light Sci. Appl.* **2019**, *8*, 27. [CrossRef] [PubMed]
4. Liu, Z.W.; Yan, S.; Liu, H.G.; Chen, X.F. Super High-Resolution Recognition of Optical Vortex Modes Assisted by a Deep-Learning Method. *Phys. Rev. Lett.* **2019**, *123*, 183902. [CrossRef] [PubMed]
5. Li, S.J.; Pan, X.Z.; Ren, Y.; Liu, H.Z.; Jing, J.T. Deterministic Generation of Orbital-Angular-Momentum Multiplexed Tripartite Entanglement. *Phys. Rev. Lett.* **2020**, *124*, 083605. [CrossRef] [PubMed]
6. Liu, S.; Lou, Y.; Jing, J. Orbital Angular Momentum Multiplexed Deterministic All-optical Quantum Teleportation. *Nat. Commun.* **2020**, *11*, 3875. [CrossRef]
7. Tamburini, F.; Anzolin, G.; Umbriaco, G.; Bianchini, A.; Barbieri, C. Overcoming the Rayleigh Criterion Limit with Optical Vortices. *Phys. Rev. Lett.* **2006**, *97*, 163903. [CrossRef]

8. Yan, L.; Gregg, P.; Karimi, E.; Rubano, A.; Marrucci, L.; Boyd, R.; Ramachandran, S. Q-plate Enabled Spectrally Diverse Orbital-Angular Momentum Conversion for Stimulated Emission Depletion Microscopy. *Optica* **2015**, *2*, 900–903. [CrossRef]
9. Hoshina, M.; Yokoshi, N.; Ishihara, H. Nanoscale Rotational Optical Manipulation. *Opt. Express* **2020**, *28*, 14980–14994. [CrossRef]
10. Bobkova, V.; Stegemann, J.; Droop, R.; Otte, E.; Denz, C. Optical Grinder: Sorting of Trapped Particles by Orbital Angular Momentum. *Opt. Express* **2021**, *29*, 12967–12975. [CrossRef]
11. Vallone, G.; D'Ambrosio, V.; Sponselli, A.; Slussarenko, S.; Marrucci, L.; Sciarrino, F.; Villoresi, P. Free-space Quantum Key Distribution by Rotation-invariant Twisted Photons. *Phys. Rev. Lett.* **2014**, *113*, 060503. [CrossRef] [PubMed]
12. Viswanathan, N.K.; Inavalli, V. Generation of Optical Vector Beams Using a Two-mode Fiber. *Opt. Lett.* **2009**, *34*, 1189–1191. [CrossRef] [PubMed]
13. Leach, J.; Yao, E.; Padgett, M.J. Observation of the Vortex Structure of a Non-integer Vortex Beam. *New J. Phys.* **2004**, *6*, 71. [CrossRef]
14. Zhang, H.; Zeng, J.; Lu, X.; Wang, Z.; Zhao, C.; Cai, Y. Review on Fractional Vortex Beam. *Nanophotonics* **2022**, *11*, 241–273. [CrossRef]
15. Zhu, L.; Tang, M.; Li, H.; Tai, Y.; Li, X. Optical Vortex Lattice: An Exploitation of Orbital Angular Momentum. *Nanophotonics* **2021**, *10*, 2487–2496. [CrossRef]
16. García-García, J.; Rickenstorff-Parrao, C.; Ramos-García, R.; Arrizón, V.; Ostrovsky, A.S. Simple Technique for Generating the Perfect Optical Vortex. *Opt. Lett.* **2014**, *39*, 5305–5308. [CrossRef]
17. Hernandez-Garcia, C.; Picon, A.; San Roman, J.; Plaja, L. Attosecond Extreme Ultraviolet Vortices from High-Order Harmonic Generation. *Phys. Rev. Lett.* **2013**, *111*, 083602. [CrossRef]
18. Sukhorukov, A.P.; Yangirova, V.V. Spatio-temporal Vortices: Properties, Generation and Recording. *Proc. SPIE* **2005**, *5949*, 594906.
19. Bliokh, K.Y.; Nori, F. Spatiotemporal Vortex Beams and Angular Momentum. *Phys. Rev. A* **2012**, *86*, 033824. [CrossRef]
20. Jhajj, N.; Larkin, I.; Rosenthal, E.W.; Zahedpour, S.; Wahlstrand, J.K.; Milchberg, H.M. Spatiotemporal Optical Vortices. *Phys. Rev. X* **2016**, *6*, 031037. [CrossRef]
21. Hancock, S.W.; Zahedpour, S.; Goffin, A.; Milchberg, H.M. Free-space Propagation of Spatiotemporal Optical Vortices. *Optica* **2019**, *6*, 1547–1553. [CrossRef]
22. Chong, A.; Wan, C.; Chen, J.; Zhan, Q. Generation of Spatiotemporal Optical Vortices with Controllable Transverse Orbital Angular Momentum. *Nat. Photonics* **2020**, *14*, 350–354. [CrossRef]
23. Bliokh, K.Y. Spatiotemporal Vortex Pulses: Angular Momenta and Spin-orbit Interaction. *Phys. Rev. Lett.* **2021**, *126*, 243601. [CrossRef] [PubMed]
24. Hancock, S.W.; Zahedpour, S.; Milchberg, H.M. Second Harmonic Generation of Spatiotemporal Optical Vortices and Conservation of Orbital Angular Momentum. *Optica* **2021**, *8*, 594–597. [CrossRef]
25. Gui, G.; Brooks, N.J.; Kapteyn, H.C.; Murnane, M.M.; Liao, C. Second-harmonic Generation and the Conservation of Spatiotemporal Orbital Angular Momentum of Light. *Nat. Photonics* **2021**, *15*, 608–613. [CrossRef]
26. Huang, S.L.; Wang, P.; Shen, X.; Liu, J. Properties of the Generation and Propagation of Spatiotemporal Optical Vortices. *Opt. Express* **2021**, *29*, 26995–27003. [CrossRef]
27. Hancock, S.W.; Zahedpour, S.; Milchberg, H.M. Mode Structure and Orbital Angular Momentum of Spatiotemporal Optical Vortex Pulses. *Phys. Rev. Lett.* **2021**, *127*, 193901. [CrossRef]
28. Cao, Q.; Chen, J.; Lu, K.; Wan, C.; Chong, A.; Zhan, Q. Sculpturing Spatiotemporal Wavepackets with Chirped Pulses. *Photonics Res.* **2021**, *9*, 2261–2264. [CrossRef]
29. Chen, J.; Wan, C.; Chong, A.; Zhan, Q. Experimental Demonstration of Cylindrical Vector Spatiotemporal Optical Vortex. *Nanophotonics* **2021**, *10*, 4489–4495. [CrossRef]
30. Chen, J.; Wan, C.; Chong, A.; Zhan, Q. Subwavelength Focusing of a Spatio-temporal Wave Packet with Transverse Orbital Angular Momentum. *Opt. Express* **2020**, *28*, 18472–18478. [CrossRef]
31. Wan, C.; Chen, J.; Chong, A.; Zhan, Q. Generation of Ultrafast Spatiotemporal Wave Packet Embedded with Time-varying Orbital Angular Momentum. *Sci. Bull.* **2020**, *65*, 1334–1336. [CrossRef] [PubMed]
32. Chen, J.; Yu, L.; Wan, C.; Zhan, Q. Spin-Orbit Coupling within Tightly Focused Circularly Polarized Spatiotemporal Vortex Wavepacket. *ACS Photonics* **2022**, *9*, 793–799. [CrossRef]
33. Mazanov, M.; Sugic, D.; Alonso, M.A.; Nori, F.; Bliokh, K.Y. Transverse Shifts and Time Delays of Spatiotemporal Vortex Pulses Reflected and Refracted at a Planar Interface. *Nanophotonics* **2022**, *11*, 737–744. [CrossRef]
34. Wang, H.; Guo, C.; Jin, W.; Song, A.; Fan, S. Engineering Arbitrarily Oriented Spatiotemporal Optical Vortices Using Transmission Nodal Lines. *Optica* **2021**, *8*, 966–971. [CrossRef]
35. Gui, G.; Brooks, N.J.; Wang, B.; Kapteyn, H.C.; Murnane, M.M.; Liao, C. Single-frame characterization of ultrafast pulses with spatiotemporal orbital angular momentum. *ACS Photonics* **2022**, *9*, 2802–2808. [CrossRef]
36. Helseth, L. Focusing of Atoms with Strongly Confined Light Potentials. *Opt. Commun.* **2002**, *212*, 343–352. [CrossRef]